Basin Research (2000) **12,** 219–226

A general inverse method for modelling extensional sedimentary basins

P. Bellingham and N. White

Bullard Laboratories, Madingley Rise, Madingley Road, Cambridge CB3 0EZ, UK

ABSTRACT

A two-dimensional inverse model for extracting the spatial and temporal variation of strain rate from extensional sedimentary basins is presented and applied. This model is a generalization of a one-dimensional algorithm which minimizes the misfit between predicted and observed patterns of basin subsidence. Our calculations include the effects of two-dimensional conduction and advection of heat as well as flexural rigidity. More importantly, we make no prior assumptions about the duration, number or intensity of rifting periods. Instead, the distribution of strain rate is permitted to vary smoothly through space and time until the subsidence misfit has been minimized. We have applied this inversion algorithm to extensional sedimentary basins in a variety of geological settings. Basin stratigraphy can be accurately fitted and the resultant spatiotemporal distributions of strain rate are corroborated by independent information about the number and duration of rifting episodes. Perhaps surprisingly, the smallest misfits are achieved with flexural rigidities close to zero. Spatiotemporal strain rate distributions will help to constrain the dynamical evolution of thinning continental lithosphere. The strain rate pattern governs the heat-flow history and so two-dimensional inversion can be used to construct accurate maturation models. Finally, our inversion algorithm is a stepping stone towards a generalized three-dimensional implementation.

INTRODUCTION

The lithospheric stretching model and its variants are used to model patterns of subsidence, crustal thinning and normal faulting in extensional sedimentary basins and on passive margins (McKenzie, 1978; Le Pichon & Sibuet, 1981; Barton & Wood, 1984). One-dimensional modelling is straightforward and can be easily carried out on well-log information or on measured stratigraphic sections (e.g. Steckler & Watts, 1978; Royden & Keen, 1980). Larger quantities of detailed one-dimensional data can be inverted as a function of temporally varying strain rate (White, 1994). A global analysis of $\sim$2000 inverted wells and sections from extended basins has yielded results which are consistent with independent information about the duration and number of rifting episodes (Newman & White, 1999). Unfortunately, a simple one-dimensional approach relies on the validity of Airy isostasy and on the location of analyses with respect to fault-bounded blocks which modify the spatial variation of synrift subsidence (e.g. Sawyer, 1986).

These shortcomings have triggered the development of two-dimensional kinematic and dynamical models. Dynamical models are based on a detailed description of the flow properties of the continental lithosphere (see references in Newman & White, 1999). For reasons that will become clear, our analysis is restricted to simpler kinematic models. Different strategies have been tried but most kinematic models include flexural rigidity and two-dimensional heat flow (e.g. Kusznir & Egan, 1989; ter Voorde & Bertotti, 1994). A typical starting point is the two-dimensional geometry of normal faulting and synrift topography, which are used to estimate the spatial variation of the lithospheric stretching factor, $\beta(x)$. In some cases, flexural rigidity is calculated directly from synrift topography (Marsden *et al.*, 1990). $\beta(x)$ is then used to predict the pattern of synrift and postrift subsidence. The fit between observed and predicted subsidence patterns can be improved by adjusting the β profile or by varying other parameters such as flexural rigidity, lithospheric thickness and basal temperature.

The fit between theory and observation is typically gauged by eye. Consequently, the accuracy and resolution of results obtained by forward modelling is difficult to assess; it is not easy to discriminate effects caused by varying or covarying different parameters. For example, how does β trade-off against poorly known parameters such as lithospheric thickness or flexural rigidity? There are more specific concerns with two-dimensional kinematic formulations: many, but not all, assume that

Correspondence: N. White, Bullard Laboratories, Madingley Rise, Madingley Road, Cambridge CB3 0EZ, UK. Tel. +44 1223 337063; e-mail: nwhite@esc.cam.ac.uk

lithospheric stretching is instantaneous (there are notable exceptions such as ter Voorde & Bertotti (1994) who use finite strain rates). This assumption considerably simplifies the two-dimensional problem and it is a crude approximation if the extension period is less than $60/\beta^2$ Myr (Jarvis & McKenzie, 1980). The major disadvantage is that temporal growth of synrift topography and stratigraphy cannot be properly modelled. Jarvis & McKenzie's rule of thumb breaks down if $\beta \geq 3$ or if the extension period is protracted, in which case highly stretched basins and passive margins cannot be modelled. From a dynamical perspective, instantaneous models are not physically realistic because they assume that strain rate is infinite.

We have addressed these concerns by developing a flexible two-dimensional inverse algorithm which can be applied to any extensional sedimentary basin or passive margin. This general model determines the spatial and temporal variation of strain rate which best fits the pattern of subsidence within a basin. Strain rate is only allowed to vary as a function of x, the distance orthogonal to the rift axis, and t, the time since rift initiation.

For the moment, we assume that the horizontal velocity does not vary with depth (i.e. $\delta u/\delta z = 0$). This 'thin sheet' approximation is justified by the spatial superimposition of synrift and postrift subsidence (*pace* Hellinger & Sclater (1983) and many others). It can easily be relaxed. Although more general kinematic and dynamical descriptions of lithospheric extension have been developed, multidimensional inversion is only computationally tractable if the forward calculation is sufficiently fast. At present, this restriction entails a simple kinematic approach which focuses on calculating basin subsidence and crustal thinning as a function of space and time. Inverted strain rate distributions are constrained to be smooth, reflecting the average deformation of the lithosphere. We have not explicitly included normal faults which modify the thickness of the upper crust on the shortest wavelengths. Future implementations will include upper crustal deformation although the results presented here will not be significantly affected.

A complete dynamical description of lithospheric extension relies on assumptions about driving forces and about lithospheric rheology, which together determine the spatial and temporal patterns of strain and strain rate. We hope to refine the dynamical constraints by measuring these patterns in a large number of basins.

FORWARD & INVERSE STRAIN RATE MODELLING

The first task is to develop a forward model which calculates the geometry of a sedimentary basin from a given spatial and temporal distribution of strain rate (Fig. 1). Our forward algorithm is divided into four steps. First, a given strain rate distribution, $G(x,t)$, and the compatibility condition are used to calculate the horizontal and vertical velocity fields, $u(x,t)$ and $v(x,z,t)$, respectively. This velocity field determines the progress of lithospheric deformation as a function of space and time. It can be shown that the stretching factor, $\beta(x,t)$, is given by

$$\frac{\partial \beta}{\partial t} + u\frac{\partial \beta}{\partial x} = \frac{\partial u}{\partial x}\beta. \quad (1)$$

In the second step, the temperature history, $T(x,z,t)$, is calculated by solving the relevant two-dimensional heat flow equation,

$$\frac{\partial T}{\partial t} + u\frac{\partial T}{\partial x} + v\frac{\partial T}{\partial z} = \kappa\left(\frac{\partial^2 T}{\partial z^2} + \frac{\partial^2 T}{\partial x^2}\right). \quad (2)$$

This second-order differential equation has horizontal and vertical advective terms which vary as a function of space and time. Since eqn 2 is coupled, it is less amenable to analytical attack and we have solved it on a finite-difference grid using a combination of the forward-time centred space (FTCS) and Lax methods (Press *et al.*, 1992).

The third step calculates changes in lithospheric density structure and hence the loading history, $L(x,t)$, from the combined temperature and deformation histories. Finally, the loading history is used to calculate the subsidence history, $S(x,t)$. The relationship between L and S depends upon D, the flexural rigidity of the lithosphere. D is often expressed in terms of τ_e, the equivalent or effective elastic thickness (Watts *et al.*, 1982). Although flexural rigidity is a preferable concept, we use elastic thickness to allow our results to be compared with previous studies. The imposition of loads on an elastic plate is solved by Fourier transform with appropriate windowing. The biggest source of uncertainty in flexural modelling is the configuration of the stress-free state. We have chosen a stress-free state which tends to favour higher values of τ_e.

This forward algorithm has been tested with a wide variety of strain rate distributions and a typical example is shown in Fig. 1. The effects of spatial and temporal strain rate variation are easily discerned. Spatial changes in strain rate generate a subsidence pattern which varies with x. Temporal changes in strain rate affect the rate of subsidence. It is important to appreciate that the cumulative amount of lithospheric stretching is determined from eqn 1 and thus depends upon the spatial and temporal pattern of strain rate. An obvious consequence is that the maximum value of β will be displaced laterally from the maximum strain rate. If τ_e is increased, the basin widens and the ratio of synrift to postrift subsidence increases at the shorter wavelengths. At basin margins, rift flank uplift becomes more pronounced (compare Fig. 1c and d).

The inverse problem seeks a solution by minimizing the difference between the predicted and observed subsidence history (Parker, 1994). For discrete and noisy data, this nonlinear problem can be solved by calculating a suite of forward models. $G(x,t)$ is first parameterized by

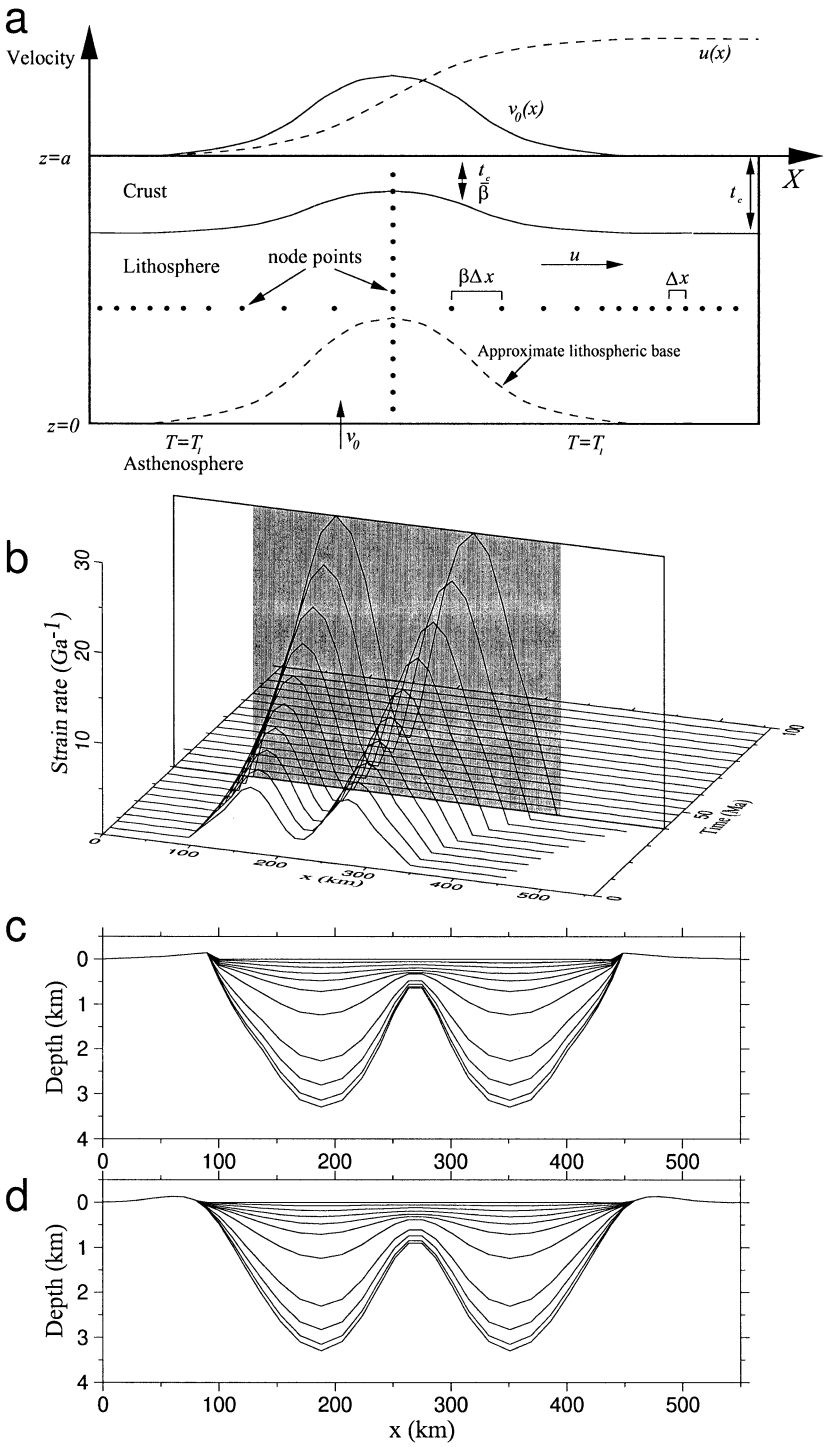

Fig. 1. Two-dimensional strain rate model. (a) Cartoon of lithosphere illustrating the principles which underlie our finite-difference scheme. For a given strain rate distribution, $G(x,t)$, the vertical and horizontal velocities, $u(x,t)$ and $v(x,z,t)$, are calculated. v decreases from v_o at the base of the lithosphere to zero at the surface. This two-dimensional velocity field is used to solve the heat-flow equation on a finite-difference grid. Boundary conditions for the linear temperature structure are $T=T_1$ at $z=0$ (base of lithosphere) and $T=0$ at $z=a$ (top of lithosphere). Vertical, horizontal and temporal node spacing is governed by Von Neumann stability criteria (Press *et al.*, 1992). Horizontal node spacing increases as a function of $\beta(x,t)$. The resultant temperature field varies through space and time. Other parameters are listed in Table 1. (b) Analytical example of strain rate variation through time and space. Strain rate varies sinusoidally in the x direction and increases exponentially over a period of 40 Myr. Spatial extent of extended basin is marked by grey rectangle. (c) Shape of sedimentary basin calculated from strain rate distribution given in (b). The different loads which vary spatially and temporally are compensated using $\tau_e=0$ km (i.e. Airy isostasy). Water-loaded basin stratigraphy is recorded every 10 Myr. Note rift flank uplift caused by lateral heat flow. (d) Same as in (c) except that loads are supported by a finite flexural rigidity ($\tau_e=5$ km). Note minor changes in stratigraphic pattern and amplification of rift flank uplift.

a set of discrete values sampled through time and space. We have then chosen to minimize a trial function, H, where

$$H=\left[\frac{1}{M}\sum_{j=1}^{M}\left(\frac{1}{N}\sum_{i=1}^{N}\left(\frac{S^{o}_{j,i}-S^{c}_{j,i}}{\sigma_i}\right)^2\right)\right]^{1/2}+\mathrm{P} \qquad (3)$$

$S^{o}_{j,i}$ and $S^{c}_{j,i}$ are the observed and predicted stratigraphy, respectively. M is the number of horizons, N is the number of data points on a each horizon, and σ_i is the uncertainty in palaeobathymetry. H is minimized by varying $G(x,t)$ which controls $S^{c}_{j,i}$. In order to stabilize the inversion, a set of weighting factors, P, are included. P ensure that the first and second derivatives of G are smooth and that G is positive. Our results are not significantly affected by changes in P. Powell's algorithm was used to minimize H (Press *et al.*, 1992).

This inverse algorithm has been applied to sets of synthetic data generated by forward modelling. Error analysis shows that the resultant strain rate distributions are significant and well resolved. The highest resolution occurs during rifting because perturbing the strain rate distribution at earlier times affects the shape of a much

Table 1. Parameters used in text. Other parameters given in White (1994).

Symbol	Parameter	Value
a	Lithospheric thickness	120–125 km
t_c	Prerift thickness of continental crust	km
G	Lithospheric strain rate	s^{-1}
u	Horizontal advective velocity	km s^{-1}
v	Vertical advective velocity	km s^{-1}
β	Stretching factor	
τ_e	Lithosperic elastic thickness	km
D	Lithospheric flexural regidity	Nm
S	Tectonic subsidence (water-loaded)	km
T	Temperature	°C
T_1	Temperature at base of lithospere	1333 °C
α	Lithospheric thermal expansion coefficient	3.28×10^{-5} $°C^{-1}$
κ	Thermal diffusivity of the lithosphere	8.04×10^{-7} m^{-2} s^{-1}

greater proportion of the calculated subsidence. Resolution decreases with time and during the last stages of postrift subsidence, strain rates are poorly resolved. In more technical terms, the *a posteriori* covariance matrix is strongly diagonal during rift periods (White, 1994). We have examined the sensitivity of results to changes in lithospheric parameters such as crustal and lithospheric thickness, density structure, and flexural rigidity (Bellingham & White, in preparation). Although there are important sources of trade-off, the calculated strain rate distributions are surprisingly robust. We are therefore optimistic that this algorithm yields geologically meaningful results.

APPLICATION

We have applied the inverse algorithm to extensional sedimentary basins from continental shelves, from continental interiors and from back-arc settings. Here, we present three examples where there are independent controls on the amount and duration of stretching. Profiles are perpendicular to the orientation of major basin structures in order to minimize the out-of-plane effects of extension and heat transport. Each profile has been modelled at least four times using values of τ_e which range from 0 to 15 km. For a given τ_e, the basin is backstripped and converted into a series of water-loaded horizons (Steckler & Watts, 1978). When larger values of τ_e are used, backstripping tends to enhance the amplitudes of short-wavelength features which are largely controlled by normal faulting. The contribution of different wavelengths can be assessed by using increasing amounts of spatial filtering to smooth out shorter wavelength variations. Since the inversion algorithm is already biased toward smooth solutions, we find that filter widths of 0–30 km do not significantly affect our results although the final misfit is improved when filter widths are large.

San Jorgé basin

The first example is the San Jorgé basin which occurs off the east coast of Argentina (Fig. 2a). This basin formed by multiple extensional episodes prior to, and coeval with, the break-up of Gondwanaland (Fitzgerald *et al.*, 1990). It is filled with predominantly shallow-marine sedimentary rocks which makes it ideal for modelling since uncertainties in palaeobathymetry are negligible. The digitized stratigraphic profile shown in Fig. 2(b) was used to determine the spatial and temporal variation of strain rate. Inverse modelling demonstrates that the observed stratigraphic horizons can be accurately matched. Significant misfit only occurs at the northern end of the basin where later uplift and denudation has modified the basin's feather edge. The resultant strain rate history, which was generated for $\tau_e = 0$ km, is complex (Fig. 2c). There are evidently two phases of extension. The earlier intense phase is confined to the centre of the basin and lasts from 140 to 120 Ma. The second phase of extension lasts from 110 to 90 Ma, has much lower strain rates, and is more spatially diffuse. Between 150 and 200 km, this second phase is continuous with the earlier event. The offset between peak strain rate and peak cumulative stretching factor is a logical consequence of the horizontal advection of lithosphere away from the fixed left-hand boundary.

The smallest misfit is obtained when the elastic thickness of the lithosphere, τ_e, is zero. If an elastic thickness of $\sim$2 km is used, small misfits are also achieved since τ_e and $G(x,t)$ can trade-off against each other. In other words, for a given τ_e, the strain rate distribution, $G(x,t)$, will adjust itself in an appropriate way. When τ_e is greater than $\sim$2 km, the resultant strain rate pattern develops a spurious spatial periodicity. This pathological behaviour is an attempt to compensate for an inappropriately large τ_e and it gives rise to a strongly fluctuating stretching profile when elastic thicknesses of 10 or 15 km are used (Fig. 2e). Thus, in spite of the trade-off between τ_e and $G(x,t)$ and the amount of spatial filtering, smallest stratigraphic misfits occur when τ_e is 2 km or less.

Independent evidence for the duration and number of rift periods can be obtained from the history of normal faulting and from the timing of volcanic activity (Faulkner, 2000). The general view is that rifting commenced during the Tithonian with activity reaching a peak during the Early Cretaceous. Figure 2(b) shows that there are, in fact, two phases of normal faulting. The first phase is concentrated towards the centre of the basin where there is excellent evidence for substantial stratigraphic growth across several faults. The second phase of faulting is concentrated between 80 and 140 km range. The existence and distribution of these phases nicely corroborate the strain rate pattern shown in Fig. 2(c). Our results suggest that there is no requirement for

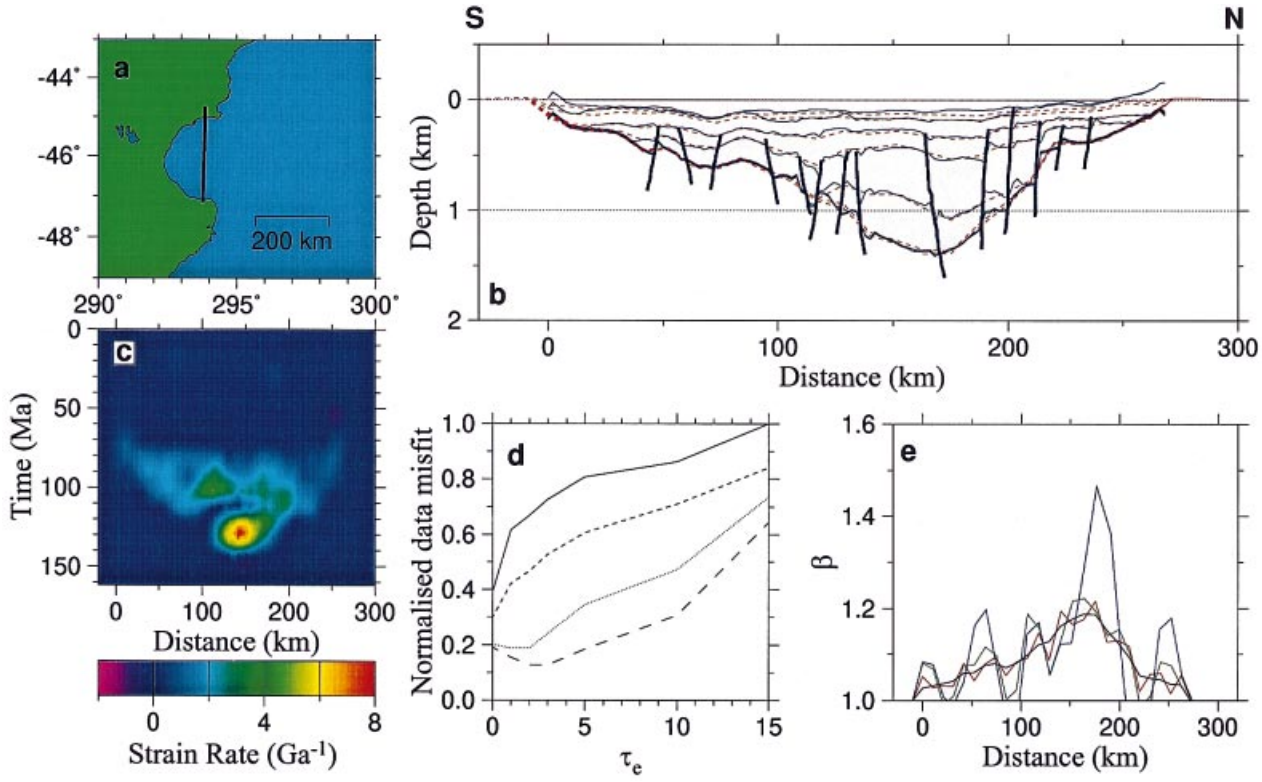

Fig. 2. San Jorgé basin, offshore Argentina. (a) Map showing location of seismic reflection profile. (b) Depth-converted and interpreted cross-section (Faulkner & White, in preparation). Thin blue lines = decompacted and water-loaded stratigraphic horizons (intra-Callovian (162 Ma), Top Valanginian (132 Ma), Top Barremian (121 Ma), intra-Cenomanian (96 Ma), Top Coniacian (86 Ma), intra-Maastrichtian (69 Ma), intra-Paleocene (58 Ma) and seabed). Before an inversion, subsidence data were water-loaded using the appropriate value of τ_e. Thick blue lines = normal faults; dashed red lines = best-fitting synthetic horizons generated by inverse modelling. Errors in palaeobathymetry were included in the inversion but they are generally small and have been omitted from the profile for clarity. (c) Spatial and temporal variation of strain rate for $\tau_e = 0$ km, which yields the synthetic horizons shown in (b). Note localized primary event at ~130 Ma and more diffuse secondary event with much lower strain rate at 100 Ma. (d) Summed and normalized data misfit plotted as a function of τ_e, the elastic thickness. For each value of τ_e, a best-fit solution was obtained and its residual misfit was recorded. Solid line uses unfiltered basin stratigraphy; short dashed line uses basin stratigraphy filtered with a cosine arch filter of 10 km width (Wessel & Smith, 1995); dotted line = 30 km filter width; long dashed line = 50 km filter width. Note that residual misfit generally decreases as τ_e decreases. Misfit also decreases as the filter width increases. (e) Final β profiles across basin for different elastic thicknesses. In each case, a 30-km filter width was used. Black line, $\tau_e = 0$ km; red line, $\tau_e = 2$ km; green line, $\tau_e = 5$ km; blue line, $\tau_e = 10$ km. Peak β is always displaced to the right of peak strain rate as a logical consequence of the lateral advection of thinning crust and lithosphere. Note dramatic and unrealistic increase in lateral variability of β when τ_e exceeds ~2 km.

strain rate to vary as a function of depth (i.e. depth-dependent stretching, lower crustal flow).

Pearl River Mouth basin

The second example is much younger and is located on the northern margin of the South China Sea (Fig. 3a). The Pearl River Mouth basin formed by extension during the Paleogene and its southern edge grades into a more highly extended passive margin (Su *et al.*, 1989). Synrift sedimentary rocks were deposited in a lacustrine environment and palaeobathymetric constraints are poor during this time period. Marine incursions occurred during latest synrift and the postrift succession was deposited in a shallow-marine environment. Uncertainties in palaeobathymetry are therefore small during the postrift phase.

As before, a series of strain rate inversions were carried out using different elastic thicknesses. The strain rate pattern for $\tau_e = 0$ km shows that modest amounts of rifting started at ~60 Ma within two separate graben (Fig. 3c). Over the next 40 Myr, these separate events intensified and merged. A peak in strain rate occurred at ~20 Ma and is located at the southern edge of the basin. This complex pattern of strain rate is the smoothest variation which results in the smallest stratigraphic misfit. The Pearl River Mouth basin demonstrates that the stratigraphic record can be fitted, albeit not as accurately as before. The smallest misfit is obtained when τ_e is less than about 2 km, regardless of how the data were filtered. Figure 3(e) shows that cumulative β is much less affected by the value of τ_e than was the case for the San Jorgé basin. This difference is not as large as it appears to be since Figs 2(e) and 3(e) have different scales.

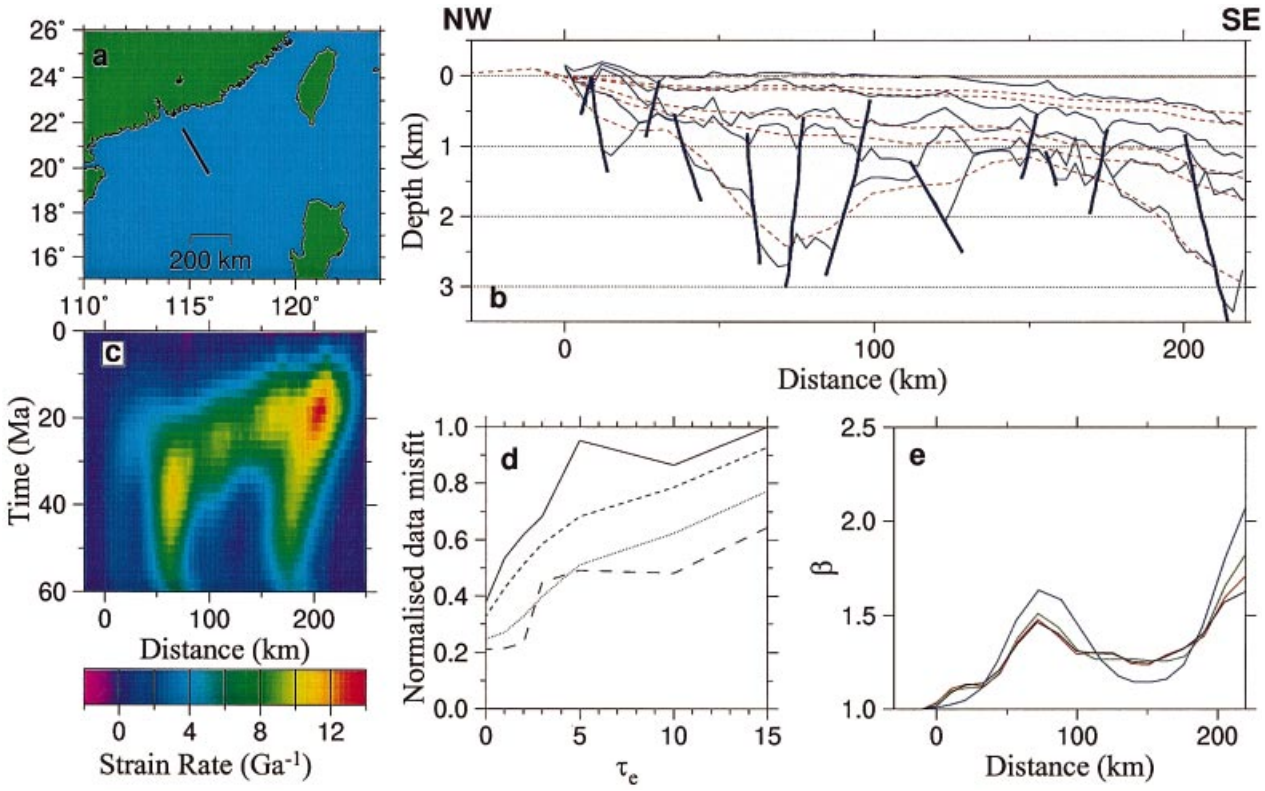

Fig. 3. Pearl River Mouth basin, South China Sea. (a) Map showing location of seismic reflection profile. (b) Depth-converted and interpreted cross-section (Wheeler & White, in preparation). Thin blue lines = decompacted and water-loaded stratigraphic horizons (intra-Paleocene (60 Ma), intra-Oligocene (28 Ma), Top Oligocene (24 Ma), intra-Miocene a (14 Ma), intra-Miocene b (12 Ma) and seabed). Thick blue lines = normal faults. Dashed red lines = best-fitting synthetic horizons generated by inverse modelling. Errors in palaeobathymetry were included in the inversion but they are generally small and have been omitted from the profile for clarity. (c) Spatial and temporal variation of strain rate for $\tau_e = 0$ km, which yields the synthetic horizons shown in (b). Note two localized primary events at 50–100 km and 150–200 km ranges. At 35 Ma, these events merge to form a widespread and intense secondary event, peaking at 20 Ma. (d) Summed and normalized data misfit plotted as a function of τ_e (see Fig. 2 for details). (e) Final β profiles across basin for different elastic thicknesses. Note that profiles do not vary significantly as a function of τ_e in contrast to Fig. 2(e).

The strain rate pattern is corroborated by the timing of extension across normal faults and by crustal thickness measurements (Wheeler, 2000). It is clear that stratigraphic growth across the principal normal faults continues until about 10 Ma. The locus of maximum strain rate between 25 and 15 Ma is coeval with the opening of a marginal oceanic basin to the south.

The Northern North Sea

Our final example is from the northern North Sea (Fig. 4a). The profile that we have chosen clearly shows the classic North Sea tilted block geometry within the East Shetland basin between 0 and 80 km. Maximum subsidence occurs within the Viking Graben between 100 and 130 km. The North Sea basin is an excellent area in which to test stretching models. Its structural development and subsidence history have been exhaustively investigated using a variety of one- and two-dimensional techniques. There are at least two phases of rifting, the best constrained occurring in Late Jurassic times. Interpretational difficulties in the pre-Jurassic section mean that the earlier Triassic extensional episode is poorly understood. Here we concentrate on modelling the Late Jurassic extensional event.

Despite large uncertainties in Cretaceous palaeobathymetry, strain rate inverse modelling produces a synthetic stratigraphic profile which closely fits the observed stratigraphy. The strain rate pattern for $\tau_e = 0$ km highlights Late Jurassic rifting especially well. Strain rate is relatively constant across the tilted fault-bounded blocks between 0 and 80 km. The Viking Graben is characterized by a strong strain rate peak at a range of $\sim$100 km. Rifting ceases at 140–130 Ma. Once again, the spatial displacement between peak strain rate and peak cumulative β by about 20 km is a function of the horizontal advection of the thinning crust.

Inverse modelling suggests that there was a mild extensional episode during the Late Cretaceous. This secondary event is localized around major basin-bounding faults on the west side of the East Shetland basin and in the Viking Graben itself. A small number of these faults cut through the Cretaceous section, although this faulting has not previously been attributed to rifting and we are

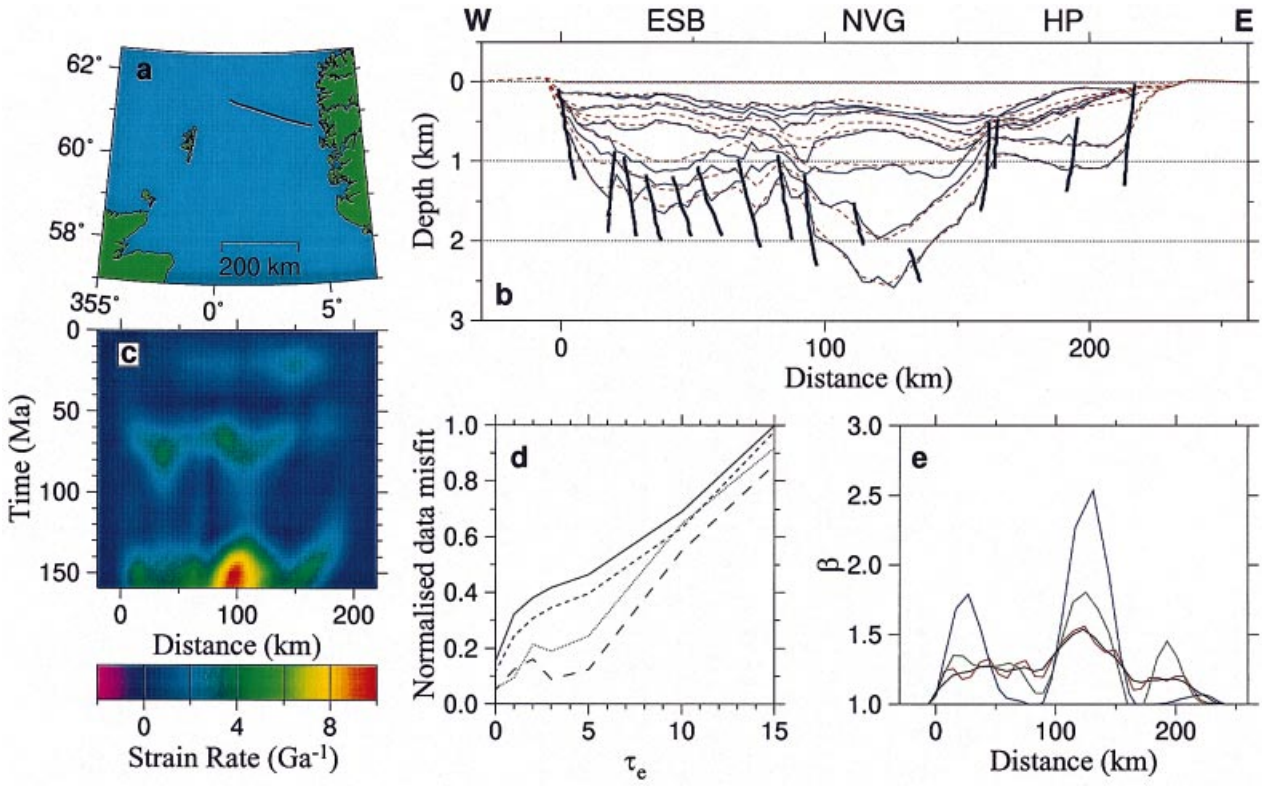

Fig. 4. Viking graben, North Sea. (a) Map showing location of seismic reflection profile. (b) Depth-converted and interpreted cross-section (Bellingham & White, in preparation). Thin blue lines = decompacted and water-loaded stratigraphic horizons (Top Callovian (159 Ma); Top Jurassic (142 Ma), Top Albian (99 Ma), Top Campanian (71 Ma), Top Cretaceous (65 Ma), Top Paleocene (55 Ma), Top Eocene (34 Ma), seabed at present-day). ESB = East Shetland Basin; NVG = North Viking graben; HP = Horda Platform. Thick blue lines = normal faults. Dashed red lines = best-fitting synthetic horizons generated by inverse modelling. Errors in palaeobathymetry, omitted for clarity, were used during inversion and they are significant (± 500 m during the Cretaceous). (c) Spatial and temporal variation of strain rate for $\tau_e = 0$ km, which yields the synthetic horizons shown in (b). Note primary event at ~ 150 Ma; highest strain rate occurs at 100 km range with lower values occurring in a band from 0 to 175 km. Diffuse secondary and tertiary events with low strain rates occur at 70 Ma and at 20 Ma but independent evidence for extension is lacking. (d) Summed and normalized data misfit plotted as a function of τ_e, the elastic thickness. See Fig. 2 for further details. (e) Final β profiles across basin for different elastic thicknesses. In each case, a 30-km filter width was used. As in Fig. 2, note dramatic increase in lateral variability of β when τ_e exceeds ~ 2 km.

not suggesting that there is an actual rift episode. However, there is excellent evidence for Middle–Late Cretaceous rifting on the Atlantic margins further north and we suggest that the thermal effects of this event are automatically being picked up by inversion. There is also an even weaker Neogene event which is not understood. In future, we hope to use the inverse approach to isolate such epeirogenic anomalies in a systematic fashion.

Our modelling shows that the elastic thickness in the northern North Sea must be less than about 3 km. As before, larger values of τ_e give rise to spurious strain rate patterns and higher misfits (Fig. 4d,e). An earlier study of the relationship between free-air gravity anomalies and load topography in the frequency domain also required $\tau_e < 5$ km (Barton & Wood, 1984).

DISCUSSION AND CONCLUSIONS

We have developed a general inverse algorithm for determining the spatial and temporal variation of strain rate in extensional sedimentary basins. This model is a generalization of White's (1994) one-dimensional model and is a significant step towards a full three-dimensional implementation. In two dimensions, the most important restriction of our scheme is that particles do not move out of the xz plane (i.e. the velocity in the y direction is zero and $\delta u/\delta y = \delta v/\delta y = 0$). Subsidence profiles should be chosen at right angles to rift trends which do not vary dramatically along strike. A further restriction is that vertical lines remain vertical at all times (i.e. $\delta u/\delta z = 0$). One or both of these restrictions can be relaxed if necessary. Our algorithm incorporates the potentially important two-dimensional effects of lateral heat flow and elastic thickness. At present, we assume that elastic thickness does not vary through time and space although, once again, this restriction can be relaxed.

The algorithm has been tested with different synthetic data, demonstrating that a variety of complex strain rate patterns are recoverable. We seek the smoothest distribution of strain rate which best fits the data and our

results are robust in the presence of random and systematic noise. A significant advantage of using an inverse approach is that the trade-off which occurs between different parameters such as lithospheric thickness, basal temperature and flexural rigidity can be examined. Thus it has become clear that we can determine an upper bound for lithospheric flexural rigidity but not a lower bound.

Here, we have applied the strain rate algorithm to three extensional sedimentary basins. In each case, observed subsidence profiles are best fitted with strain rate distributions which are consistent with independent geological information about rifting events. Flexural rigidities are small: in each case the equivalent elastic thickness, τ_e, is less than ~ 2 km. Higher values of τ_e progressively degrade the fit between theory and observation, yield geologically unrealistic strain rate distributions and cause large-amplitude fluctuations in stretching factors. These effects are apparent even when short-wavelength variations (< 10 km) have been removed by filtering.

There is much debate about the elastic thickness of continental lithosphere and we are conscious that the values we obtain imply that continental lithosphere has negligible flexural rigidity as it extends and cools. We have simply sought the smoothest solution which best fits the data; it is unlikely that temporal increases or decreases in elastic thickness would significantly improve this quality of fit. Short-wavelength topography predominates during rift phases and provides the best constraints on elastic thickness. During postrift phases, the subsidence pattern is dominated by longer wavelengths and so elastic thickness is less well resolved. In our view, subsidence observations are generally too noisy to extract temporal and spatial variations in elastic thickness.

In one dimension, a global data set of inverted subsidence data provided interesting dynamical insights (Newman & White, 1999). We believe that spatiotemporal patterns of strain rate variation will further constrain dynamical models of lithospheric deformation. A concerted effort to apply the two-dimensional algorithm to Phanerozoic basins worldwide is now underway.

ACKNOWLEDGMENTS

P.B. was supported by the Cambridge Arctic Shelf Program, ExxonMobil, Saga, and the Department of Earth Sciences. P. Faulkner and P. Wheeler generously allowed us to show their unpublished results. We also thank J. Haines, S. Jones, J. Maclennan, R. Scott and H. Walford. Paul Heller, Patience Cowie and an anonymous reviewer provided very helpful reviews.

REFERENCES

Barton, P. & Wood, R. (1984) Tectonic evolution of the North Sea basin: crustal stretching and subsidence. *Geophys. J. Royal Astron. Soc.*, **79,** 987–1022.

Faulkner, P. (2000) Basin formation in the South Atlantic Ocean. PhD Dissertation, University of Cambridge.

Fitzgerald, M.G., Mitchum, R.M., Uliana, M.A. & Biddle, K.T. (1990) Evolution of the San Jorge basin. *Argentina. Am. Ass. Petrol. Geol. Bull.*, **74,** 879–920.

Hellinger, S.J. & Sclater, J.G. (1983) Some comments on two-layer extensional models for the evolution of sedimentary basins. *J. Geophys. Res.*, **88,** 8251–8269.

Jarvis, G.T. & McKenzie, D.P. (1980) Sedimentary basin formation with finite extension rates. *Earth Planet. Sci. Lett.*, **48,** 42–52.

Kusznir, N.J. & Egan, S.S. (1989) Simple-shear and pure-shear models of extensional sedimentary basin formation: application to the Jeanne d'Arc Basin, Grand Banks of Newfoundland. In: *Extensional Tectonics and Stratigraphy of the North Atlantic Margins* (Ed. by A.J. Tankard & H.R. Balkwill), *Am. Ass. Petrol. Geol., Mem.*, **46,** 305–322.

Le Pichon, X. & Sibuet, J.-C. (1981) Passive margins: a model of formation. *J. Geophys. Res.*, **86,** 3708–3720.

Marsden, G., Yielding, G., Roberts, A.M. & Kusznir, N.J. (1990) Application of a flexural cantilever simple-shear/pure-shear model of continental lithosphere extension to the formation of the northern North Sea basin. In: *Tectonic Evolution of the North Sea Rifts* (Ed. by D.J. Blundell). & A.D. Gibbs, pp. 240–261. Clarendon Press.

McKenzie, D.P. (1978) Some remarks on the development of sedimentary basins. *Earth Planet. Sci. Lett.*, **40,** 25–32.

Newman, R. & White, N.J. (1999) The dynamics of extensional sedimentary basins: constraints from subsidence inversion. *Phil. Trans. Royal Soc., London*, **357,** 805–830.

Parker, R.L. (1994) *Geophysical Inverse Theory*. Princeton University Press, Princeton.

Press, W.H., Teukolsky, S.A., Vetterling, W.T. & Flannery, B.P. (1992) *Numerical Recipes in Fortran 77: the Art of Scientific Computing*, 2nd edn. Cambridge University Press.

Royden, L. & Keen, C.E. (1980) Rifting processes and thermal evolution of the continental margin of eastern Canada determined from subsidence curves. *Earth Planet. Sci. Lett.*, **51,** 343–361.

Sawyer, D. (1986) Effects of basement topography on subsidence history analysis. *Earth Planet. Sci. Lett.*, **78,** 427–434.

Steckler, M.S. & Watts, A.B. (1978) Subsidence of the Atlantic-type continental margin off New York. *Earth Planet. Sci. Lett.*, **41,** 1–13.

Su, D., White, N., McKenzie, D. (1989) Extension and subsidence in the Pearl River Mouth Basin, northern South China Sea. *Basin Res.*, **2,** 205–222.

ter Voorde, M. & Bertotti, G. (1994) Thermal effects of normal faulting during rifted basin formation, 1. A finite difference model. *Tectonophysics*, **240,** 133–144.

Watts, A.B., Karner, G.D. & Steckler, M.S. (1982) Lithospheric flexure and the evolution of sedimentary basins. *Phil. Trans. Royal Soc., London*, **305,** 249–281.

Wessel, P. & Smith, W.H.F. (1995) New, Version of the Generic Mapping Tools released. *EOS Trans. Am. Geophys. Union*, **76,** 329.

Wheeler, P.J. (2000) Basin formation in Southeast Asia. PhD Dissertation, University of Cambridge.

White, N.J. (1994) An inverse method for determining lithospheric strain rate variation on geological timescales. *Earth Planet. Sci. Lett.*, **122,** 351–371.

Received 1 April 2000; revision accepted 29 August 2000.